SiPM Single Photon Time Resolution Measurement

Author
Lai Gui

Supervised by
Guido Haefeli
Federico Ronchetti

Laboratoire de Physique des Hautes Énergies
École Polytechnique Fédérale de Lausanne

June 6, 2025
Physics Project II - PHYS-422

Abstract

In this study, we present a comparative analysis of the Single Photon Time Resolution (SPTR) of various Silicon Photomultipliers (SiPMs), including multichannel SiPM arrays from Hamamatsu and FBK, as well as single-channel SiPMs. Using a breakdown of the measured full width at half maximum (FWHM) into contributions from jitter, trigger, laser, and other intrinsic factors, we characterise and contrast the performance across different SiPMs. The analysis demonstrates that FBK SiPMs, particularly the FBKW342004_µLens, show superior SPTR performance due to features like microlens focusing that minimise intrinsic timing spread. Hamamatsu SiPMs show consistent and competitive performance, while single-channel SiPMs exhibit larger FWHM values, partly due to their susceptibility to thermal noise and weaker signal-to-noise ratios. These findings provide a basis for further refinement in SiPM design and usage, especially in time-critical photon detection applications.

1 Introduction

Silicon Photomultipliers (SiPMs) play a vital role in modern High Energy Physics (HEP) experiments due to their high single-photon detection efficiency, excellent timing performance, compact size, and robustness against radiation damage. Among these characteristics, the timing resolution is particularly critical, as it directly impacts time-of-flight (TOF) measurements. TOF information is essential for reconstructing particle momentum and, consequently, for particle identification.

In this context, our objective is to measure the Single Photon Time Resolution (SPTR) of a SiPM, which represents its timing precision when detecting only one photon — the scenario that yields the poorest timing resolution. As the number of detected photons increases, the timing resolution improves due to better signal statistics.

By accurately determining the worst-case SPTR, we can better evaluate and compare the performance of different SiPM models, enabling informed choices for specific detector applications where precise timing is required.

1.1 What is an SiPM?

A Silicon Photomultiplier (SiPM) is a solid-state photodetector composed of an array of microcells, each of which is a Single-Photon Avalanche Diode (SPAD), as illustrated in Fig.1. Each SPAD operates under a bias above its breakdown voltage. This mode of operation is known as Geiger mode, as shown in Fig.2.

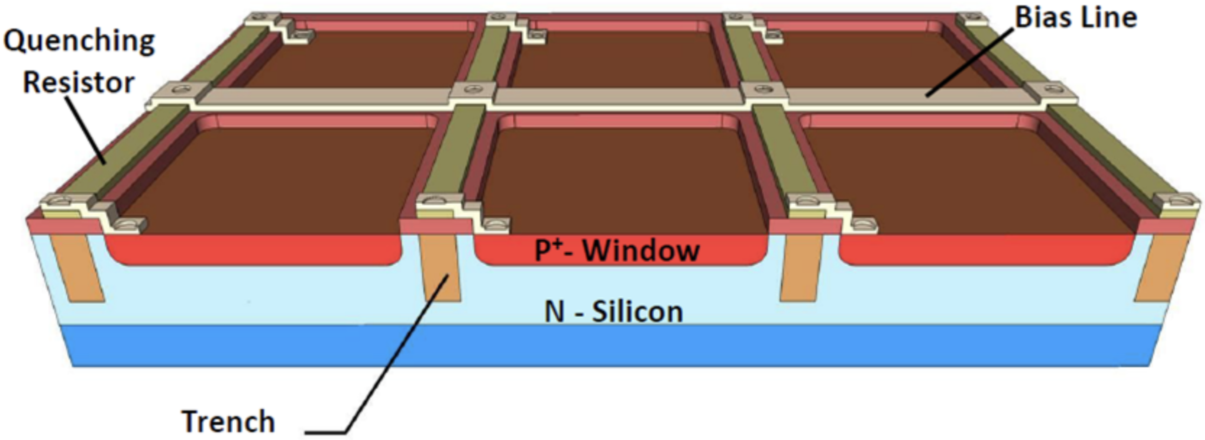

Figure 1: [1] SiPMs are composed of arrays of SPAD (Single-Photon Avalanche Diode) microcells. Each microcell includes a quenching resistor, a bias line, and a p^+ window on an n silicon substrate. Trenches between cells provide optical isolation to minimise crosstalk.

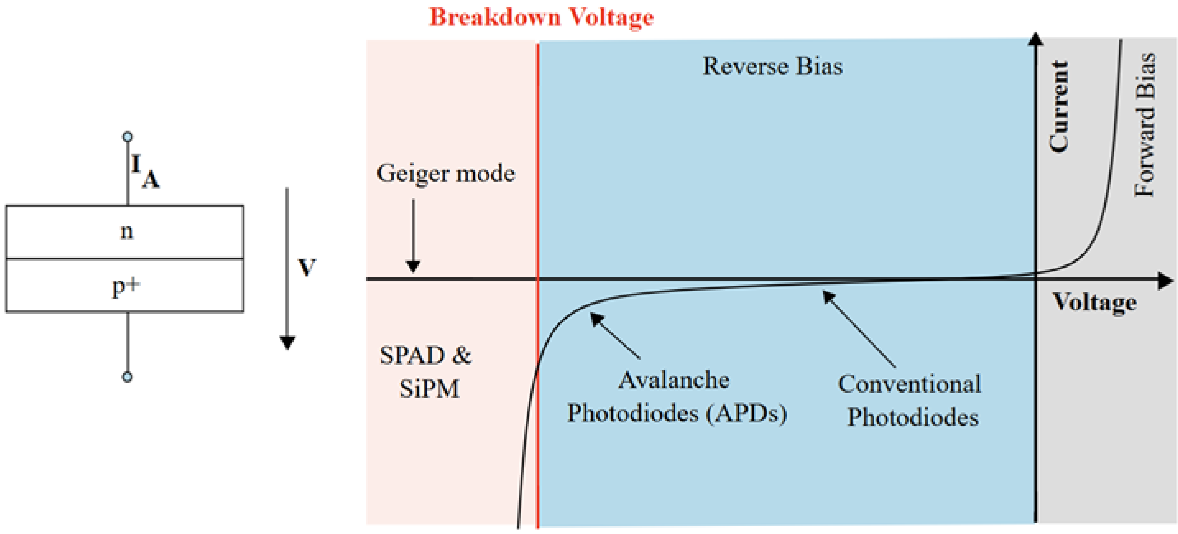

Figure 2: [2] Current–voltage characteristic of a SPAD microcell. In Geiger mode, the SPAD is operated with a reverse bias exceeding its breakdown voltage, enabling avalanche multiplication upon the detection of a single photon.

When operating below breakdown voltage (i.e., in linear APD mode), only electrons, being less massive and more mobile than holes, typically contribute significantly to impact ionisation as they drift toward the cathode. However, in Geiger mode, once the reverse bias is set above the breakdown voltage, holes drifting toward the anode also gain enough energy to produce secondary electron-hole pairs. This mutual ionisation leads to a self-sustaining avalanche current.

Because this avalanche process does not stop on its own once triggered, each SPAD includes a quenching resistor. This resistor momentarily limits the current and reduces the bias voltage below breakdown, thereby halting the avalanche and allowing the microcell to reset and be ready for the next detection.

When photons strike different SPAD microcells, they independently trigger avalanches. The output signal of the SiPM is the analog sum of the currents from all fired microcells, making the total output roughly proportional to the number of detected photons. However, when the incident light intensity is high, a significant fraction of the SPADs may fire simultaneously, leading to saturation — a non-linear response where the SiPM no longer reliably reflects the true light intensity.

1.2 Single Photon Time Resolution

The *Single Photon Time Resolution* (SPTR) characterises the temporal spread of the SiPM's response to single-photon events. It reflects the device's ability to reconstruct the photon's time-of-arrival, which is crucial in applications such as track and vertex reconstruction in high-energy physics detectors.

Several physical and instrumental factors contribute to the SPTR of a SiPM. The five primary sources of timing uncertainty are detailed below:

1. Intrinsic spread: due to non-uniformities in the electric field within each SPAD microcell, the timing response varies depending on where within the cell the photon is absorbed. The electric field is strongest near the centre of the microcell, where carriers are more rapidly accelerated, resulting in a faster response. This spatial variation leads to a spread in detection times. This effect can be partially mitigated by using microlens arrays to focus incoming photons toward the centre of each microcell, thus minimising the response variation. Other effects, such as differences in the structure of individual SPADs due to manufacturing processes, can also contribute to the intrinsic spread.

2. Transit time skew: because the signal readout path is not equally distant from all microcells, avalanches initiated in SPADs physically closer to the output line arrive slightly earlier than those farther away. This introduces a systematic spatial bias in the timing. This effect can be studied experimentally by selectively masking parts of the SiPM and comparing the response timing of microcells at varying distances from the readout path.

3. Trigger time spread: the laser used in the experiment emits a synchronisation signal (trigger) that marks the nominal photon emission time. The timing of the SiPM signal is measured relative to this trigger. However, in our setup, the trigger itself has an associated uncertainty of less than 20 ps, though the exact value was not independently measured in this study.

4. Laser statistics: In addition to trigger uncertainty, the laser pulse itself exhibits temporal spread with respect to the trigger signal. For the laser model and power level used in this experiment, the timing spread is approximately 56 ps. This intrinsic property of the laser contributes directly to the overall SPTR.

5. Jitter error: Random noise in the electronics chain also introduces timing uncertainty, often referred to as jitter. This effect becomes more pronounced when the signal amplitude is small, as the timing becomes more sensitive to fluctuations. This effect can be visualised in Fig. 3. The contribution of jitter can be quantitatively estimated using the standard deviation of the baseline noise and the slope of the leading edge of the signal waveform, as laster described in Sec. 2.2.3.

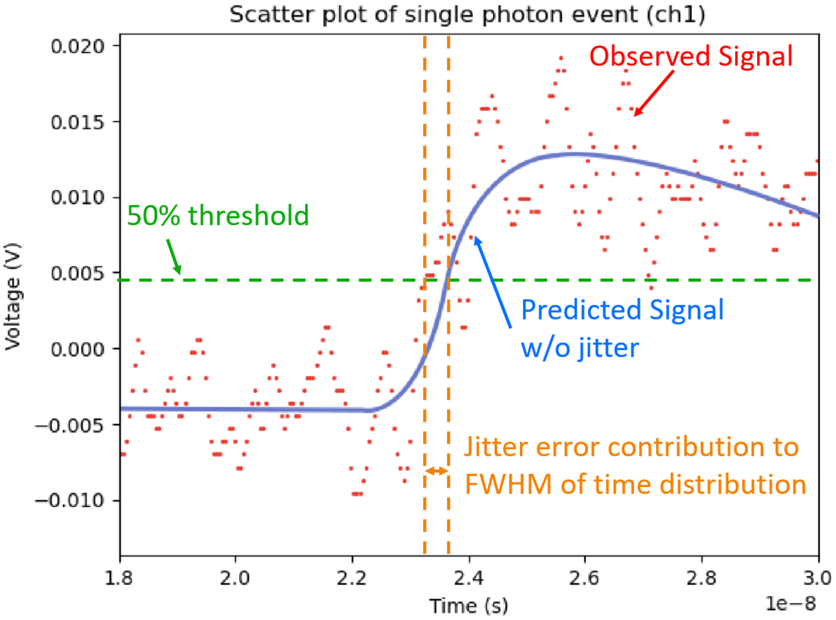

Figure 3: Illustration of jitter-induced timing error. Random fluctuations in the signal waveform cause deviations in the threshold crossing point, leading to uncertainty in the measured time.

1.3 SiPM Parameters

SiPMs produced by different manufacturers can exhibit varying characteristics. Several key parameters influence their Single Photon Time Resolution (SPTR) performance:

1. Pixel size: smaller pixels result in reduced p–n junction capacitance, enabling faster signal rise times. Although smaller pixels typically have lower Photon Detection Efficiency (PDE), this mainly affects photon detection statistics and is therefore not a limiting factor in SPTR-focused measurements.

2. Number of microcells: while this does not directly influence SPTR, a larger number of microcells means some are located further from the readout circuitry, potentially increasing the contribution of transit time skew.

3. Overvoltage (OV): defined as the reverse bias voltage exceeding the breakdown voltage. A higher overvoltage increases the electric field strength within the SPADs, promoting faster avalanche initiation and steeper signal rise, thus improving SPTR. However, excessive OV also raises the dark count rate due to increased thermal generation, which can degrade timing resolution through enhanced jitter.

4. Quenching resistor design: the parameters and design of the quenching resistor influence the recovery time of each microcell and the overall shape of the output signal. Both factors impact SPTR, especially under high-rate conditions.

5. Temperature: lower operating temperatures reduce thermal noise, which can lead to modest improvements in SPTR by suppressing noise-induced jitter. Additionally, as the gain of a SiPM is temperature-dependent, maintaining a controlled temperature helps stabilise the gain and can also contribute to jitter error reduction.

2 Methodology

The main objectives of this project are divided into three key tasks:

1. Collect waveform data from various SiPMs operated at different overvoltages (OV);
2. Identify single-photon events within the data, ideally selecting clean events that are not superimposed on thermal noise residuals;
3. Analyse the timing distribution at which the voltage of single-photon events crosses a defined threshold.

The procedures used to accomplish each of these tasks are detailed in the following subsections.

2.1 Experimental Setup

An illustration of the experimental setup is shown in Fig. 4. A laser source and bias power supply are directed into a shielded box, which protects against external electromagnetic noise and light. Inside the box, the SiPM under test is placed. The SiPM signals are routed through a readout board and amplified by a 40 dB amplifier before being digitised by an oscilloscope. The acquired data are then transmitted to and stored on a computer for subsequent analysis.

Prior to data acquisition, the breakdown voltage of each SiPM channel is determined by linear extrapolation of the signal amplitude as a function of bias voltage, measured by varying the bias around the nominal breakdown voltage.

In most measurements, the SiPM overvoltage (OV) is scanned from 2 to 9 V in 0.5 V increments. For some SiPM models capable of withstanding higher bias, the OV range is extended up to 12 V.

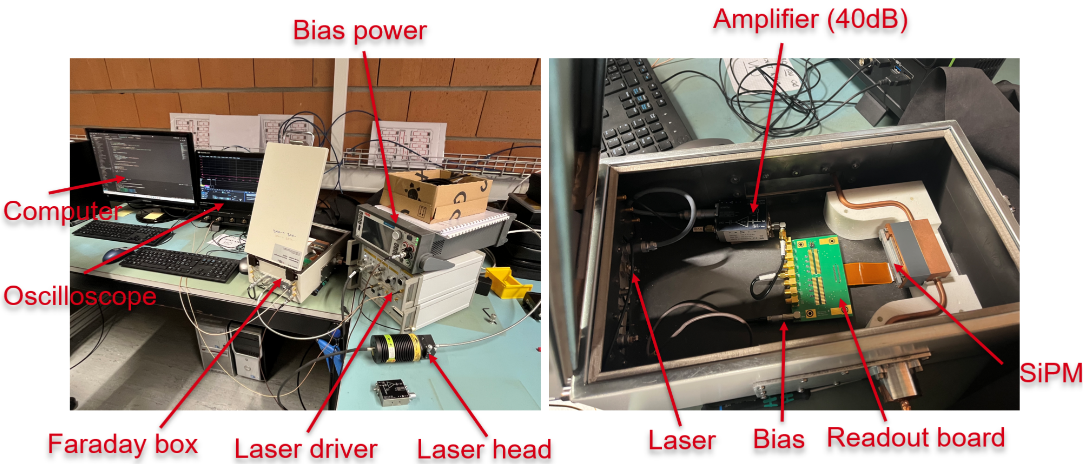

Figure 4: **Left**: the experimental setup consists of a computer, oscilloscope, Faraday box, laser driver with laser head, and bias power supply. **Right**: inside the Faraday box, the SiPM under test is connected to a readout board and a 40 dB amplifier. During data collection, laser pulses are triggered and directed onto the SiPM, while the SiPM signals are amplified, digitised by the oscilloscope, and transmitted to the computer for storage and further analysis.

The readout board acquires signals from only one SiPM channel at a time, ensuring that no current flows in adjacent channels and thereby preventing crosstalk effects.

It is worth noting that photon reflections inside the Faraday box can introduce additional systematic errors in the time resolution measurements. This effect is investigated in Appendix A. To mitigate this issue, a black foam tube is used to absorbs the photons not propagating directly towards the SiPM.

2.2 Analysis Method

2.2.1 Separation of Events

Single-photon events need to be separated from background noise and multiple-photon events. To achieve this, a time window is applied to the waveforms within which the maximum amplitude of each event is extracted, as illustrated in Fig. 5a, with FBKW942087 channel 69 at 2.0 OV as an example.

The maximum amplitudes of events within this time window are then compiled into a histogram, shown in Fig. 5b. The distinct peaks in the histogram correspond to background, single-photon, and multiple-photon events, enabling their clear categorisation.

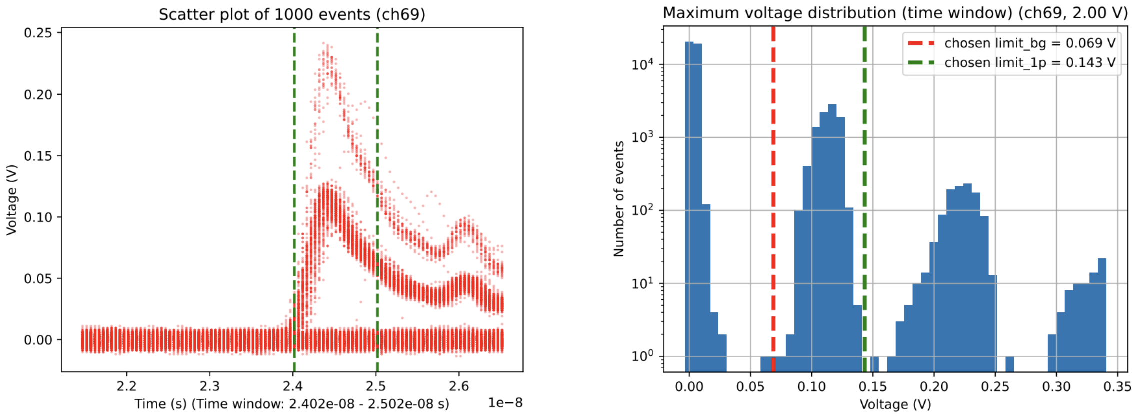

(a) (b)

Figure 5: (a) For this specific case, the time window for extracting the maximum amplitude is chosen between 24.02 and 25.02 ns. Selecting this interval prevents random fluctuations outside the signal region from affecting the event selection. (b) The histogram of maximum amplitudes exhibits distinct peaks. Events with maximum amplitudes in the range 0.069 to 0.143 V are identified as single-photon events.

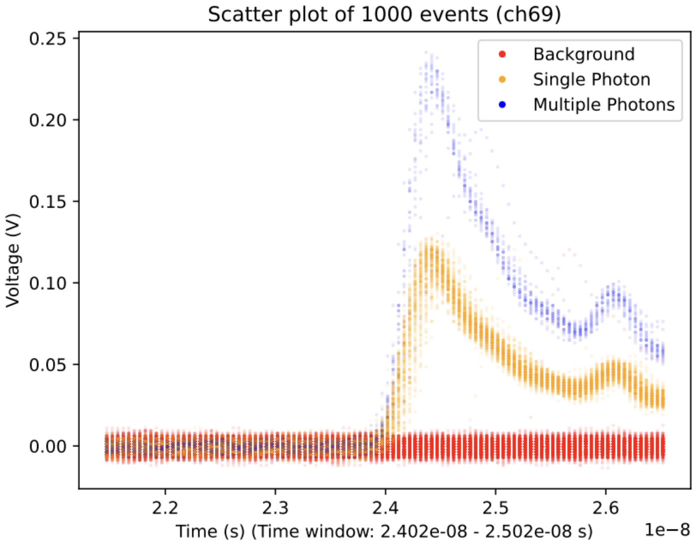

Figure 6: Classification of event types based on the maximum amplitude within the time window shown in Fig. 5a. Events are labeled as *Background* (noise or no photon detection), *Single Photon* (events corresponding to a single photon detection), or *Multiple Photons* (events with multiple simultaneous photon detections).

Based on the amplitude histogram, different types of events can be classified according to different peaks, as illustrated in Fig. 6. These categories include background noise, single-photon events, and multiple-photon events. For the purposes of this study, the analysis will be exclusively focused on the *Single Photon* events, as they provide the fundamental limit on the SiPM's timing resolution. The baseline is obtained by averaging the amplitudes of background events, and is then subtracted from the single-photon waveforms to isolate the intrinsic SiPM response to single photons.

2.2.2 Fitting of Time Distribution

Before constructing the histogram for the time distribution, it is important to consider the bin width limitation imposed by the oscilloscope's sampling characteristics. Since the sampling times are uniformly distributed within each sampling interval, the bin size must be chosen carefully to ensure that the resulting timing distribution can be meaningfully interpreted and fitted.

For a uniform distribution over the interval (a, b), the standard deviation is given by [3]:

$$\sigma = \sqrt{\frac{(b-a)^2}{12}}. \tag{1}$$

In our setup, the oscilloscope has a sampling interval of 50 ps, which corresponds to a uniform distribution with a standard deviation of approximately 14.43 ps.

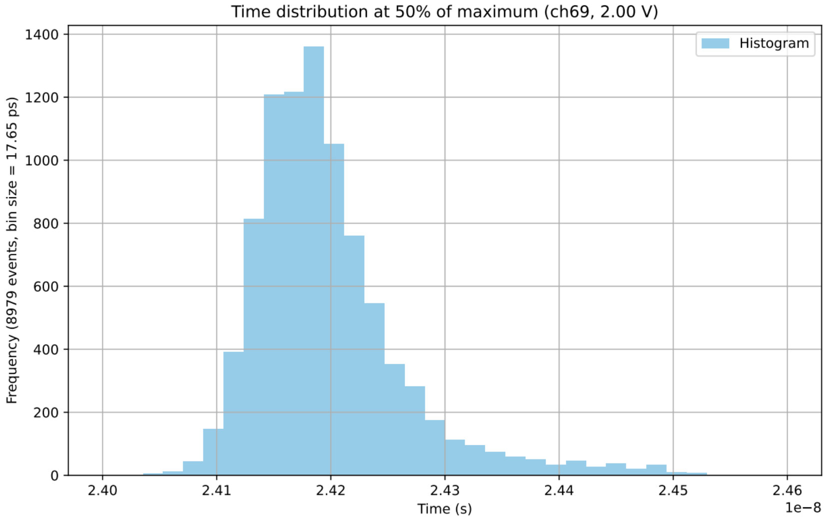

Figure 7: Time distribution of Single Photon events reaching 50% of their maximum amplitudes. The bin size of 17.65 ps ensures meaningful physical interpretation.

Taking this into account, the time distribution of the single-photon events can be constructed, as shown in Fig. 7. The time values are recorded by linearly interpolating between the two points closest to a specified fraction (threshold) of the maximum amplitudes of individual waveforms.

To more accurately extract the full width at half maximum (FWHM) of the distribution, the fitting model of *Exponentially Modified Gaussian* (EMG) is applied, with the function:

$$f(x;\mu,\sigma,\lambda) = \frac{\lambda}{2}\exp\left[\frac{\lambda}{2}\left(2\mu+\lambda\sigma^2-2x\right)\right]\operatorname{erfc}\left(\frac{\mu+\lambda\sigma^2-x}{\sqrt{2}\sigma}\right) , \tag{2}$$

where the complementary error function is defined as

$$\operatorname{erfc}(x) = 1-\operatorname{erf}(x) = \frac{2}{\sqrt{\pi}}\int_x^\infty e^{-t^2}\,dt \ . \tag{3}$$

This distribution resembles a Gaussian (bell) curve but exhibits a longer tail on the positive side, as illustrated in Fig. 8.

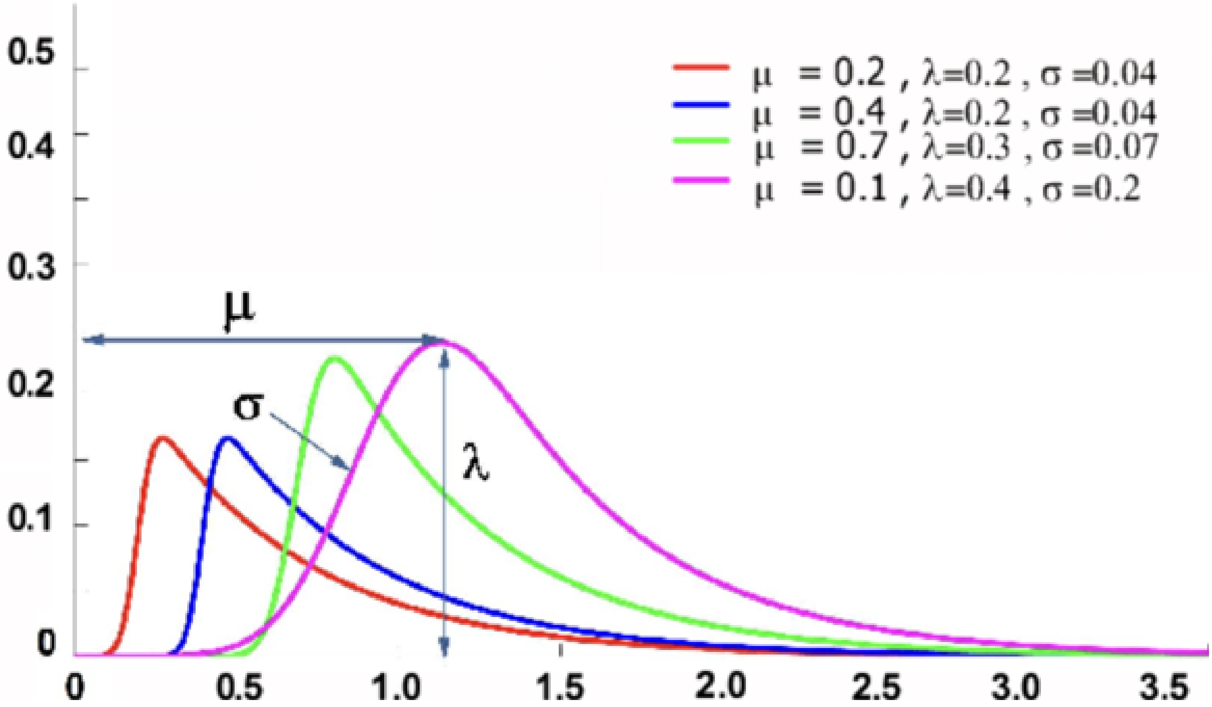

Figure 8: [4] Exponentially Modified Gaussian (EMG) distributions illustrating the effects of varying the parameters μ, λ, and σ, which correspond to the peak position, the exponential decay rate (affecting the tail length), and the peak width, respectively.

The fitting of the time distribution is hence performed using the EMG model, as illustrated in Fig. 9. From this fit, a rather accurate approximation of the FWHM is extracted, which serves as a key metric for the SPTR measurement.

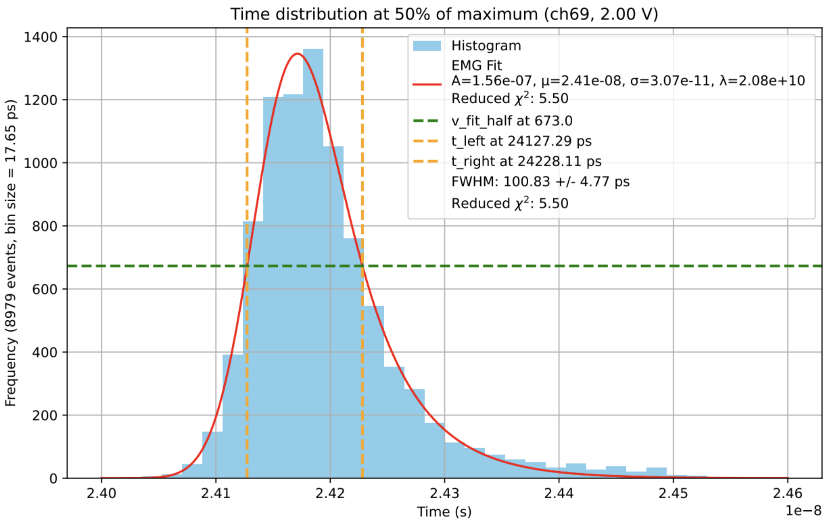

Figure 9: By fitting the EMG model, the FWHM of the time distribution can be estimated, along with its associated uncertainty. In this case, the fitted FWHM is 100.83 ± 4.77 ps, with a reduced chi-squared value of 5.5, indicating that the EMG is appropriate for describing the distribution.

This fitting procedure is repeated for various threshold levels, resulting in a distribution of FWHM values as a function of the chosen threshold, as shown in Fig. 10. The errors on the FWHM values are derived solely from the statistical uncertainties provided by the `scipy.curve_fit` fitting routine. Therefore, these error estimates may not fully account for other potential systematic uncertainties present in the measurement or data processing, which could affect the overall accuracy of the results.

For FBKW942087 channel 69, the process is repeated for different overvoltages (OV), therefore the distribution shown in Fig. 11 can be constructed. It is observed that at low OV values, the FWHM decreases as the OV increases. This improvement saturates around 8.0 V, beyond which further increases in OV do not significantly reduce the FWHM.

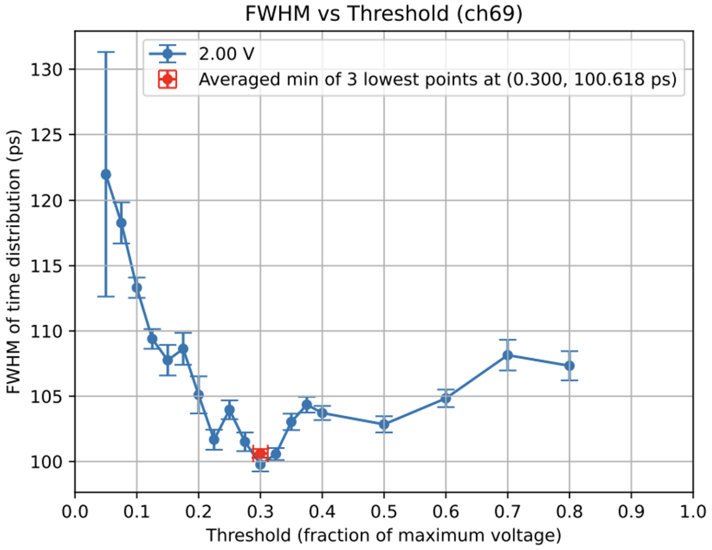

Figure 10: The fitting procedure is repeated for different threshold values at the chosen thresholds. By averaging the three data points corresponding to the lowest FWHM values, a characteristic FWHM can be obtained for this specific overvoltage (OV), as well as the threshold at which this minimum FWHM occurs.

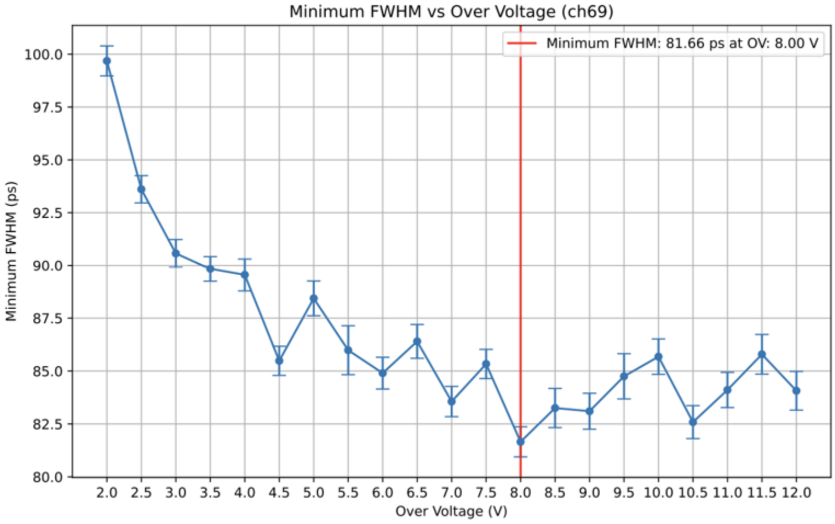

Figure 11: Correlation between the minimal FWHM and overvoltage (OV) for this channel. The FWHM decreases with increasing OV up to a minimum at approximately 8.0 V, beyond which saturation occurs and no further improvement is observed.

This process is repeated for multiple channels, and their average value is calculated to obtain the SPTR of the SiPM array. An example of such an averaged result is shown in Fig. 12 for the FBKW942087 SiPM.

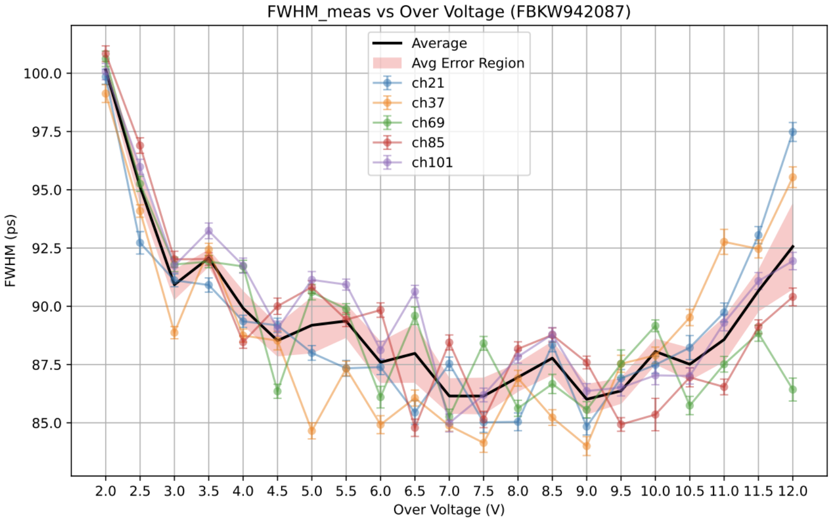

Figure 12: Average measured FWHM from five different channels of the FBKW942087 SiPM. All channels exhibit similar behaviour, showing a common saturation in FWHM improvement beyond an overvoltage of 8.0 V.

2.2.3 FWHM Contributions Analysis

The contribution of jitter error to the FWHM of the time distribution can be estimated using the following expression:

$$\mathrm{FWHM}_{\mathrm{jitter}} = 2.3458 \times \frac{\sigma_{\mathrm{background}}}{\text{average gradient}}, \tag{4}$$

where the coefficient 2.3458 corresponds to the relationship between the standard deviation and FWHM of a Gaussian distribution, which is assumed to describe the background noise.

For the case shown in Fig. 10, the distribution of $\mathrm{FWHM}_{\mathrm{jitter}}$ is presented in Fig. 13. Using the previously averaged threshold value at which the minimal FWHM occurs, the corresponding $\mathrm{FWHM}_{\mathrm{jitter}}$ can be interpolated accordingly.

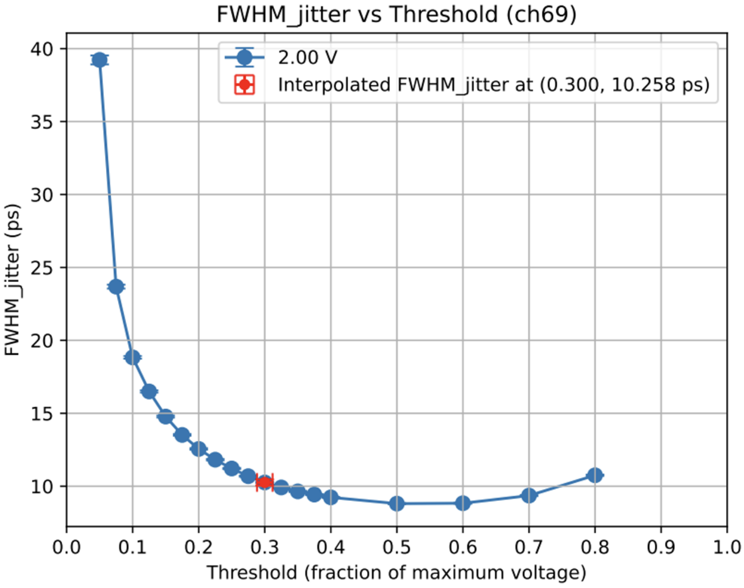

Figure 13: Jitter error is inversely proportional to the signal gradient, therefore reaches a minimum near the 50% threshold, where the signal slope is typically the steepest, as expected.

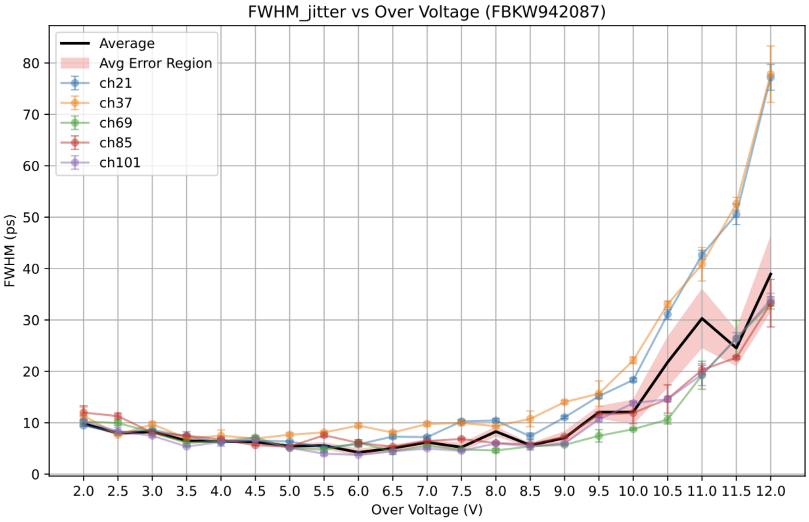

Figure 14: Average $\mathrm{FWHM}_{\mathrm{jitter}}$ for FBKW942087 across different channels. Note that channels 21 and 37 exhibit higher jitter errors compared to the other three channels, which may be attributed to them belonging to different SiPM dies of the SiPM.

Similarly to the previous analysis, the average of the $\mathrm{FWHM}_{\mathrm{jitter}}$ can be calculated across multiple channels for the FBKW942087 SiPM. This averaged jitter contribution is presented in Fig. 14, providing insight into the typical impact of electronic noise on the timing resolution for this device.

The noticeably higher jitter error observed in channels 21 and 37 may be attributed to them belonging to different SiPM dies of the SiPM compared to the other channels. This variation in jitter could arise from subtle non-uniformities in the fabrication process, such as variations in the microcell geometry, differences in quenching resistor parameters, or slight inhomogeneities in the doping concentration and therefore electric field distribution across the microcells. To fully understand these effects and their impact on jitter error, more detailed investigations, including comparison across multiple SiPM samples, are necessary.

To separate the different contributions discussed in Sec. 1.2, the following relation is used:

$$\mathrm{FWHM}^2_{\mathrm{meas}} = \mathrm{FWHM}^2_{\mathrm{jitter}} + \mathrm{FWHM}^2_{\mathrm{trigger}} + \mathrm{FWHM}^2_{\mathrm{laser}} + \mathrm{FWHM}^2_{\mathrm{others}} \ , \tag{5}$$

where $\mathrm{FWHM}_{\mathrm{others}}$ represents a combined contribution of the intrinsic spread and transit time skew, which cannot be individually resolved with our current experimental setup.

Among these contributions, the laser timing uncertainty is well characterised and average at $\mathrm{FWHM}_{\mathrm{laser}} = 56\,\mathrm{ps}$ for all OV values, allowing straightforward subtraction. The trigger timing uncertainty, $\mathrm{FWHM}_{\mathrm{trigger}}$, is reported to be less than 20 ps, hence is treated as an asymmetric error affecting the lower bound of the measured FWHM.

After accounting for the jitter, trigger, and laser contributions, the average $\mathrm{FWHM}_{\mathrm{others}}$ component can be extracted for FBKW942087, shown in Fig. 15.

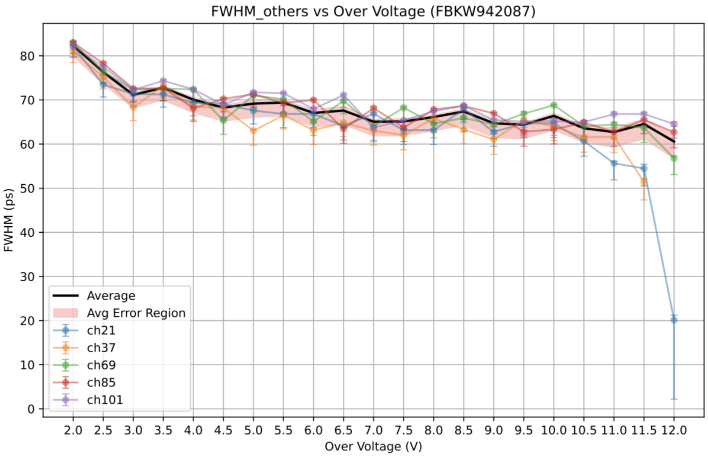

Figure 15: Average $\mathrm{FWHM}_{\mathrm{others}}$ for FBKW942087 across different channels. At higher Over Voltages, channels 21 and 37 exhibit lower $\mathrm{FWHM}_{\mathrm{others}}$ values.

Overall, the channels show good agreement, indicating consistent intrinsic and transit time skew contributions. However, at higher Over Voltages, channels 21 and 37 exhibit noticeably lower $\mathrm{FWHM}_{\mathrm{others}}$ values, which correlates with their increased $\mathrm{FWHM}_{\mathrm{jitter}}$ observed previously.

2.2.4 Background Filtering

For some SiPMs, such as the one illustrated in Fig. 16, a single readout channel is connected to a significantly larger number of SPAD cells compared to the configurations discussed earlier. This design choice typically aims to increase the overall photon detection area and improve the dynamic range, enabling the detection of higher light intensities, but may also introduce additional complexities such as increased capacitance and potential variations in timing performance across the combined microcells.

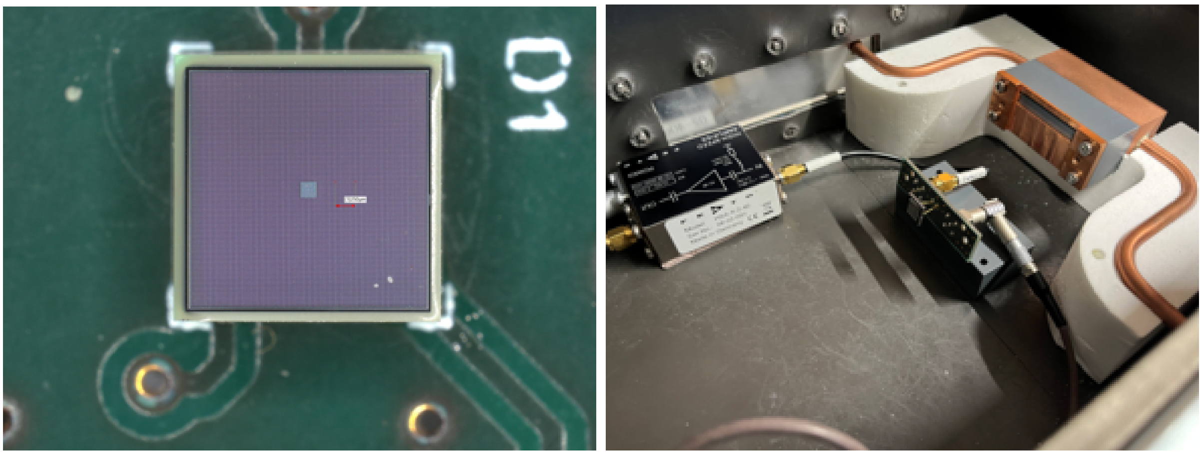

(a)

(b)

Figure 16: (a) A photo of the S14160_3 SiPM. This device is significantly larger than the Hamamatsu and FBK SiPMs, featuring only a single readout channel despite its increased active area. (b) The SiPM is mounted onto a compact readout board designed to facilitate signal acquisition and integration with the measurement setup.

It is observed that for this type of SiPM, the signal amplitude is comparable to the background noise level. This situation is illustrated in Fig. 17. The distinction between background, single photon, and multiple photon events is much less clear compared to the well-separated peaks observed in Fig. 5b for FBKW942087. This underlines a substantial overlap in the amplitude distributions of different event categories, making it difficult to distinguish single-photon events based on histogram peak separation.

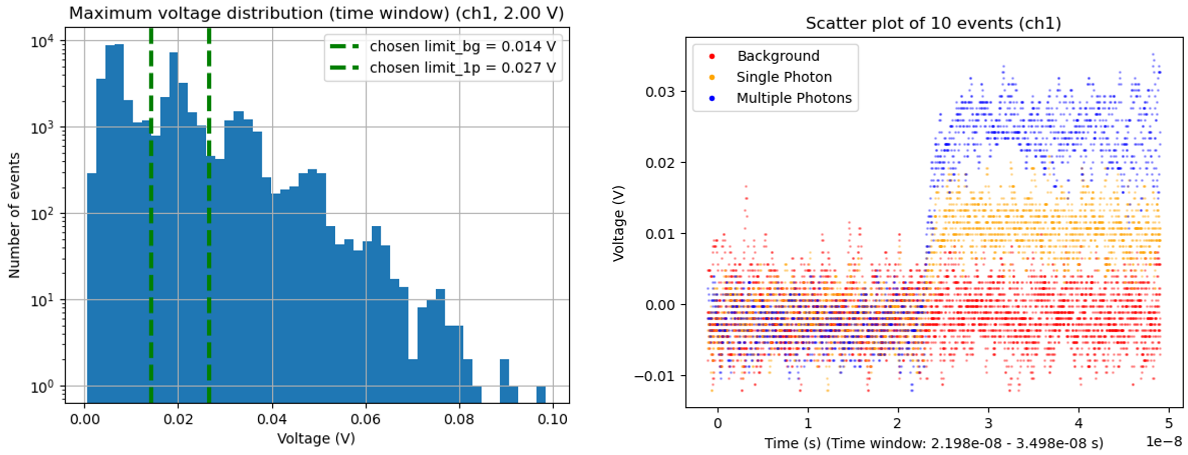

(a) (b)

Figure 17: (a) Histogram of maximum voltages for the single-channel SiPM before filtering. While peaks corresponding to different photon events are visible, they appear continuous and poorly separated, making event classification difficult. (b) Example waveforms from the single-channel SiPM. The signal pulses are closely packed, with the amplitude of random noise being comparable to that of single photon signals, complicating clear event identification.

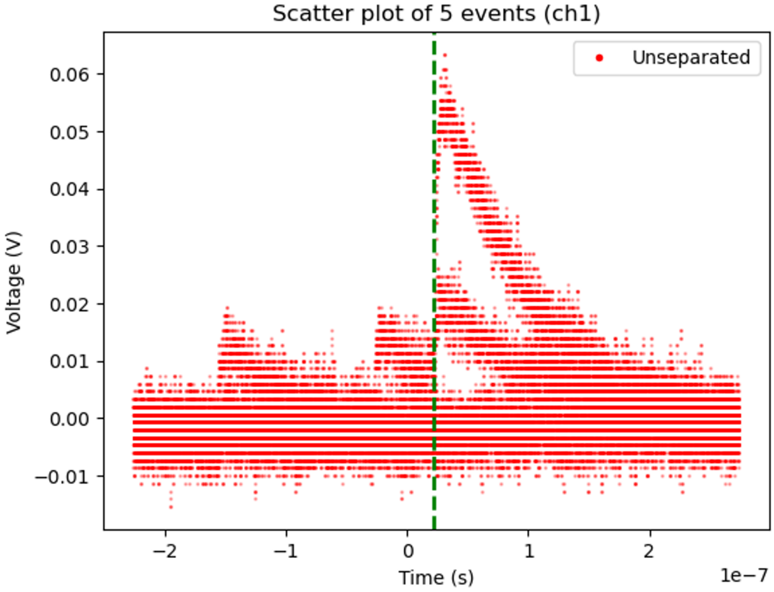

Figure 18: Example waveform of the single channel SiPM after enlarging the data acquisition time window. It is evident that some signals are superimposed on the residual thermal noise baseline, which has not fully recovered prior to the signal onset.

This effect is considered to be a consequence of some signal pulses being superimposed on the residual thermal noise. By enlarging the time window for waveform acquisition, as illustrated in Fig. 18, it becomes evident that portions of the noise baseline have not fully recovered before the signal is triggered, which contributes to the difficulty in distinguishing single photon events.

To mitigate the influence of residual thermal noise on signal characterisation, a *voltage filtering* method is introduced. This involves analysing a portion of the waveform that precedes the signal onset (specifically, the left region of Fig. 18) to assess the baseline behaviour. A histogram of the maximum voltage within this pre-signal region is constructed, as shown in Fig. 19a. The first distinct peak in this distribution is taken to represent uncontaminated baseline noise.

Using this subset of ”clean” waveforms, the histogram of maximum signal voltages within the target signal window is therefore constructed. The resulting distribution, shown in Fig. 19b, demonstrates noticeably improved peak separation compared to the unfiltered case in Fig. 17a, allowing for more reliable identification of single photon and multi-photon events.

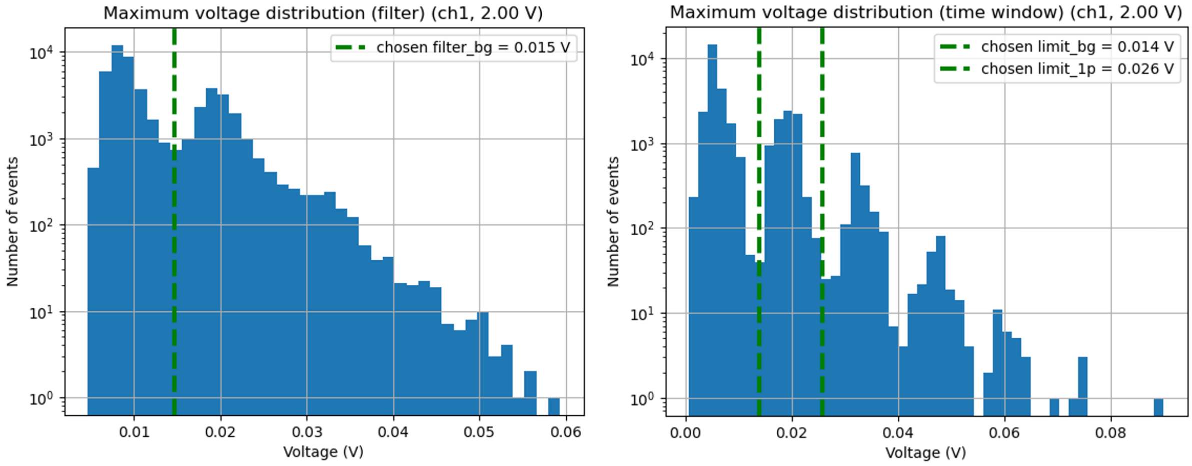

(a)

(b)

Figure 19: (a) Histogram of the maximum voltage in the pre-signal region of each waveform. Only the events clustered around the first peak is selected, which we interpret as ”clean” events unaffected by residual thermal noise. (b) Histogram of the maximum voltages within the defined time window, reconstructed using only the clean events. Compared to the unfiltered case in Fig. 17a, the spectral peaks are now more clearly separated, enabling more reliable photon event classification.

Using the filtered dataset, classification the events can again be performed based on their maximum amplitudes, similar to the method applied previously. The resulting waveforms for the selected Single Photon events are shown in Fig. 20. In this case, the influence of thermal noise is significantly reduced. Specifically, we no longer observe any residual fluctuations in the region preceding the signal onset. The following analysis is then performed as previously described in Sec. 2.2.2 and Sec. 2.2.3.

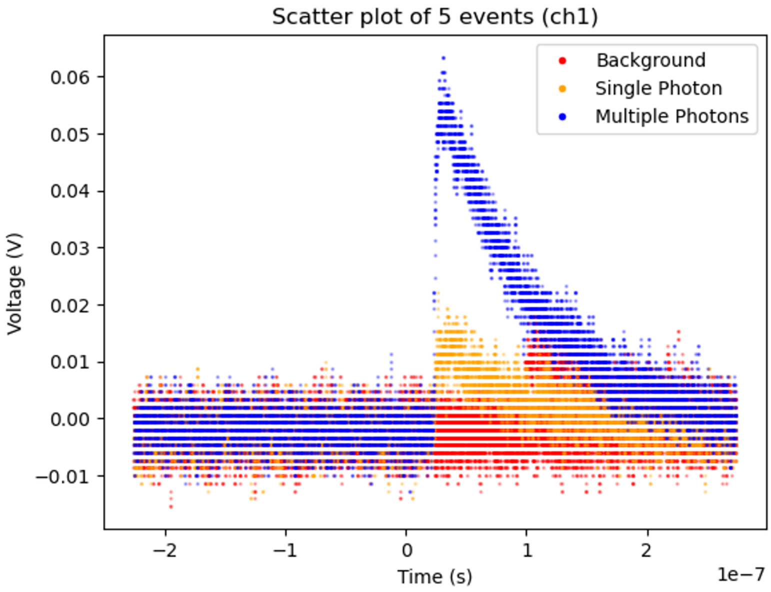

Figure 20: Separated filtered waveforms. In this case, no residual thermal noise is observed in the region before the signal onset, indicating successful removal of contaminated events through the voltage filtering process.

3 Results & Discussion

3.1 Hamamatsu SiPMs: H202450038 and H202442058

The collective results for two Hamamatsu SiPMs: H202450038 and H202442058, are summarised in Fig. 21. Although these two devices differ slightly in pixel size — H202450038 has a pixel size of $50 \times 50\,\mu\text{m}^2$, while H202442058 uses $42 \times 42\,\mu\text{m}^2$ — their Single Photon Time Resolution (SPTR) performance is remarkably similar.

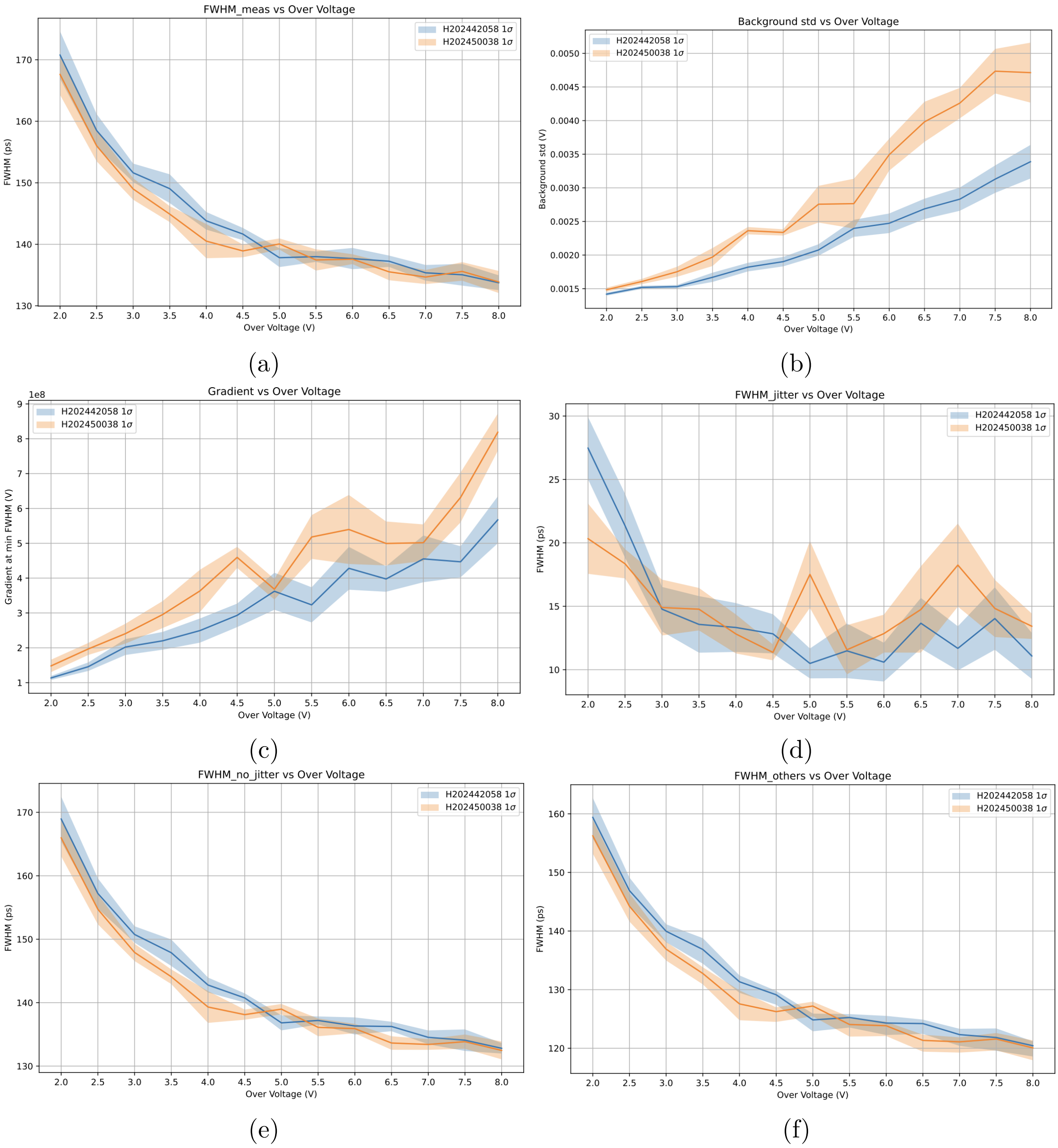

(a) (b) (c) (d) (e) (f)

Figure 21: Average results across different channels of H202450038 and H202442058. Despite having different pixel sizes, the two Hamamatsu SiPMs exhibit very similar SPTR performance across all evaluated metrics.

Each subplot in the figure represents one key metric evaluated as a function of overvoltage (OV):

(a) FWHM$_{\mathbf{meas}}$: The measured Full Width at Half Maximum (FWHM$_{\text{meas}}$) values for both SiPMs are closely aligned across the OV range, indicating comparable overall timing performance.

(b) Background σ: H202450038 exhibits a slightly higher standard deviation in the background signal. This could be due to differences in device layout, noise characteristics, or coupling with readout electronics.

(c) Signal Gradient: Interestingly, H202450038 also shows a consistently higher average signal gradient. This compensates for the higher noise in the jitter calculation.

(d) FWHM$_{\mathbf{jitter}}$: Since jitter is calculated as the ratio of background noise to signal gradient, the increased noise and steeper gradient in H202450038 cancel out, resulting in similar jitter contributions for both devices.

(e) FWHM$_{\mathbf{no\ jitter}}$ & (f) FWHM$_{\mathbf{others}}$: As a consequence of the comparable trends in both measured FWHM and jitter error, the jitter-corrected FWHM (i.e., FWHM$_{\text{no jitter}}$) and the extracted FWHM$_{\text{others}}$ also display similar behaviour. This consistency confirms that the two SiPMs share broadly similar intrinsic and systematic timing characteristics.

These results validate the reproducibility and reliability of Hamamatsu's SPTR performance across devices with minor pixel geometry variations.

3.2 FBK SiPMs: FBK942087 and FBK342004_µLens

The comparative results for FBK942087 and FBK342004_µLens are shown in Fig. 22. The latter includes a microlens array designed to focus incoming photons more effectively onto the centres of the microcells, which helps reduce intrinsic timing spread.

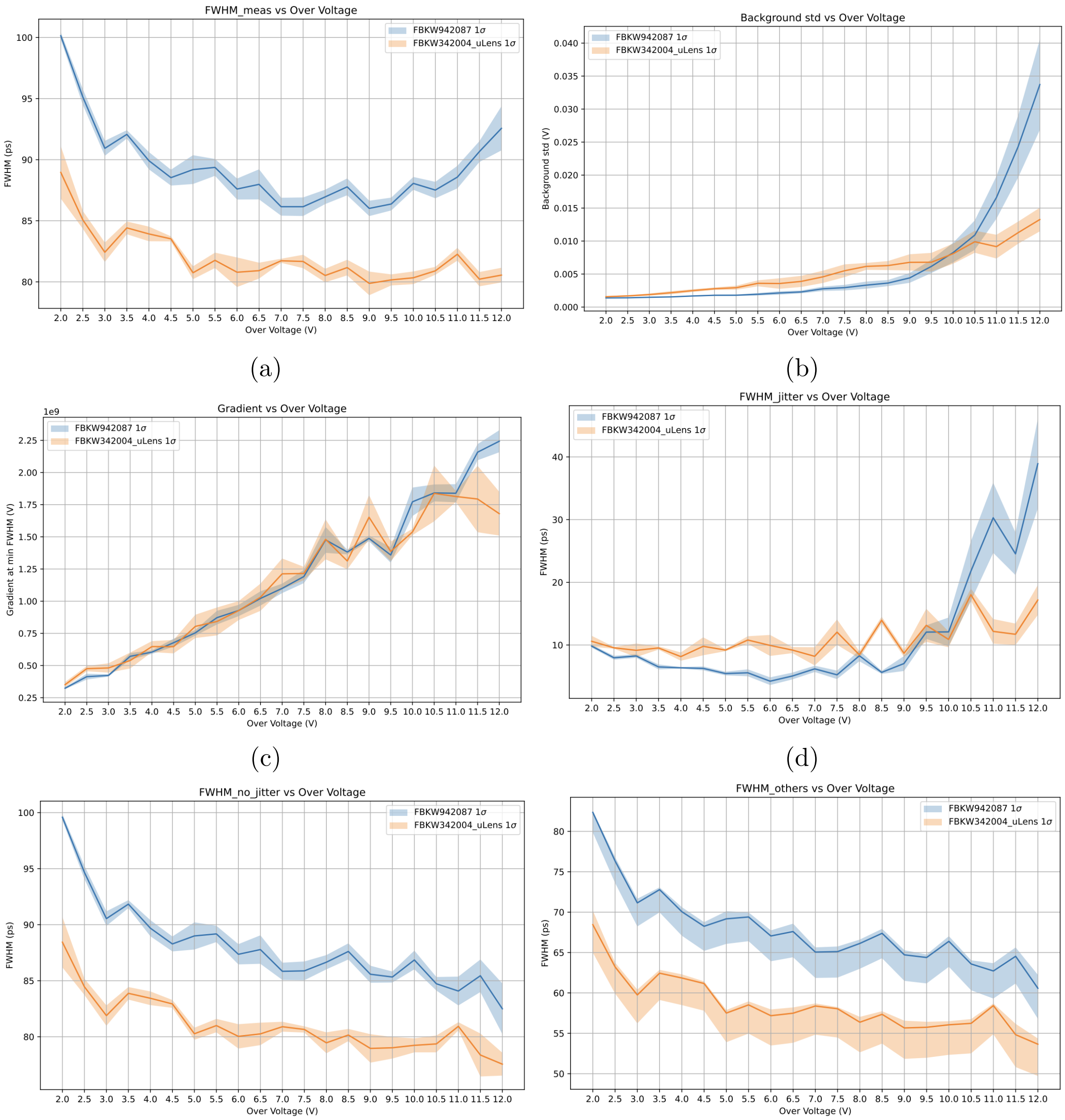

(a) (b)

(c) (d)

(e) (f)

Figure 22: Average results across different channels of FBK942087 and FBK342004_µLens. While both devices reach $\text{FWHM}_{\text{meas}}$ saturation beyond 7 V, FBK342004_µLens consistently performs better by about 5 ps across the OV range. The microlens design contributes to reduced intrinsic timing error and improved SPTR.

Each subplot corresponds to one measured quantity:

(a) $\mathbf{FWHM_{meas}}$: Both SiPMs exhibit saturation in $\mathrm{FWHM_{meas}}$ after approximately 7 V OV. However, FBK342004_µLens consistently outperforms FBK942087 across the entire OV range by about 5 ps. Additionally, FBK942087 shows a rise in $\mathrm{FWHM_{meas}}$ beyond 9.5 V.

(b) Background σ: The background standard deviation is initially similar for both devices, but FBK942087 shows a sharp increase after 9.5 V, eventually exceeding that of FBK342004_µLens.

(c) Signal gradient: The signal gradients for both SiPMs are similar throughout the OV range, indicating comparable signal rise characteristics.

(d) $\mathbf{FWHM_{jitter}}$: Due to the elevated background noise, FBK942087 shows a noticeable increase in $\mathrm{FWHM_{jitter}}$ after 9.5 V, surpassing that of FBK342004_µLens.

(e) $\mathbf{FWHM_{no\ jitter}}$ & (f) $\mathbf{FWHM_{others}}$: After correcting for jitter contributions, both SiPMs exhibit flat saturation behaviour. FBK342004_µLens maintains a 5 ps advantage, attributable to its microlens array, which reduces intrinsic error by improving photon focus onto the centers of the microcells.

The FBK SiPM with microlens is designed to focus incoming photons towards the centers of the microcells. This is beneficial because the electric field strength is highest in these central regions, which facilitates faster triggering of the avalanche process. As a result, this design helps reduce the intrinsic timing jitter and improves the overall single photon timing resolution (SPTR).

3.3 Single Channel SiPMs: S13360_2, S14160_3 and S13360_6

Notice that the labelled numbers for these SiPMs are only indicative, as we observed that the actual device parameters do not perfectly match the names on their corresponding base mounts. Among these three devices, only the S13360_6 is treated with the filtering technique described previously in Sec. 2.2.4.

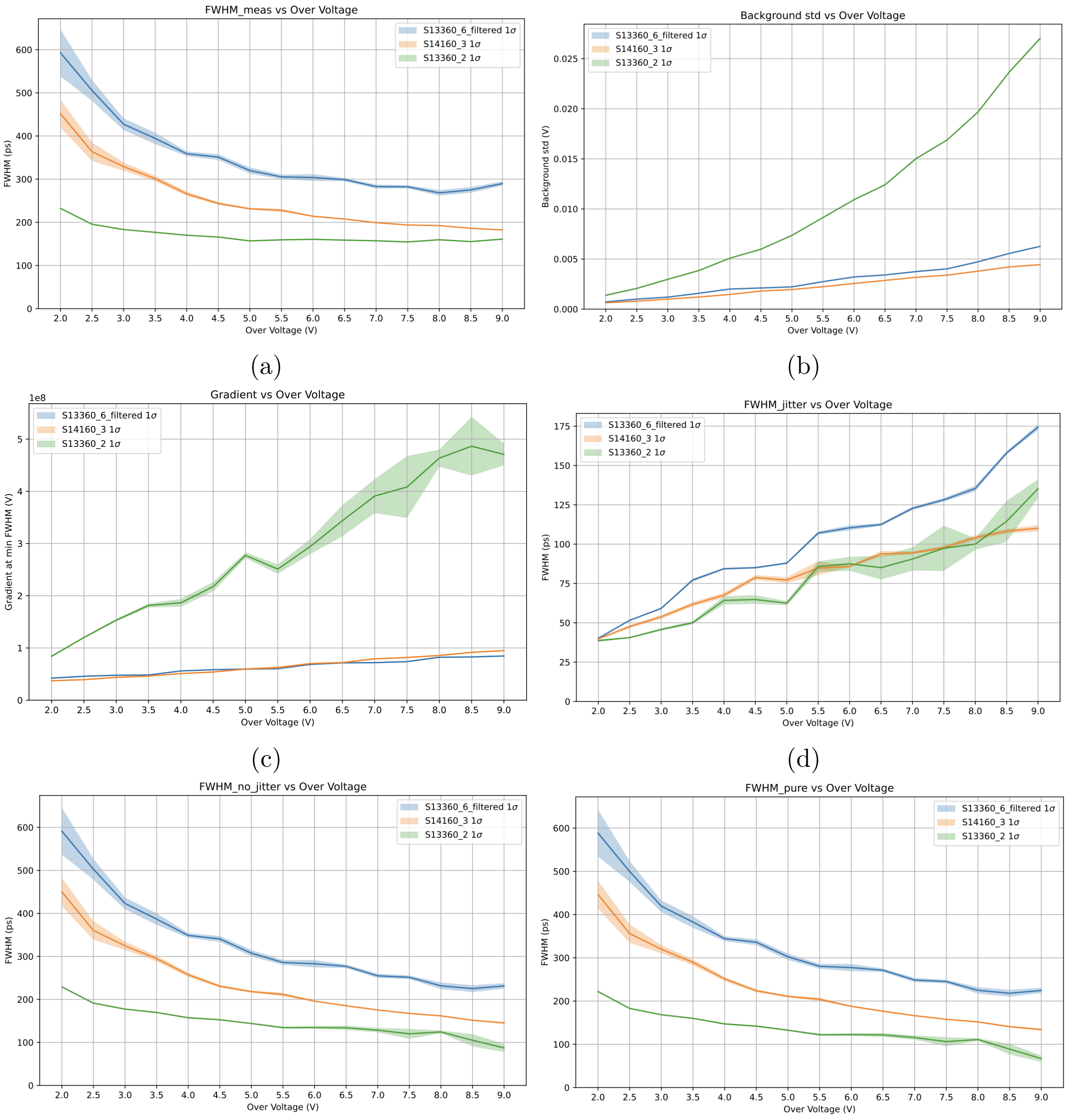

(a) (b) (c) (d) (e) (f)

Figure 23: Average results across different channels for single channel SiPMs S13360_2, S14160_3, and S13360_6 (filtered). The labelled device numbers are indicative only. Among them, only S13360_6 is treated with the filtering technique to reduce thermal noise effects.

Each subplot corresponds to one measured quantity:

(a) $\mathbf{FWHM_{meas}}$: The overall $\mathrm{FWHM_{meas}}$ for the three SiPMs follows the order S13360_6_filtered > S14160_3 > S13360_2. The S13360_2 reaches saturation early around 5.0 V of overvoltage (OV), whereas the other two do not show a clear saturation even towards the maximum tested OV of 9.0 V.

(b) Background σ: The background standard deviation for S13360_6_filtered behaves similarly to that of S14160_3. In contrast, S13360_2 exhibits a much faster increase in background noise with OV.

(c) Signal gradient: Similar to the background noise trend, the gradient for S13360_2 increases more rapidly, while S13360_6_filtered and S14160_3 show comparable behaviours.

(d) $\mathbf{FWHM_{jitter}}$: Being the ratio of background standard deviation to the gradient, the jitter contribution shows similar trends for all three SiPMs. However, S13360_2 consistently exhibits larger errors compared to the other two devices.

(e) $\mathbf{FWHM_{no\ jitter}}$ and (f) FWHM_pure: After removing the jitter contribution, both these quantities steadily decrease with increasing OV for all three SiPMs, without obvious saturation. Nonetheless, the ranking remains the same: S13360_6_filtered has the highest values, followed by S14160_3, and then S13360_2 with the lowest.

Across the measured parameters, S13360_2 generally shows the best timing performance and earlier saturation in $\mathrm{FWHM_{meas}}$, while S13360_6_filtered has the highest FWHM values. Background noise and gradient trends mirror each other, leading to similar jitter contributions, though S13360_2 exhibits larger errors. After accounting for jitter, all devices show improvement without clear saturation, maintaining the relative performance order.

3.4 Comparison Across All SiPM Types

A comparative overview of the timing performances across the different SiPM groups — FBK, Hamamatsu, and Single Channel SiPMs — is presented in Fig. 24.

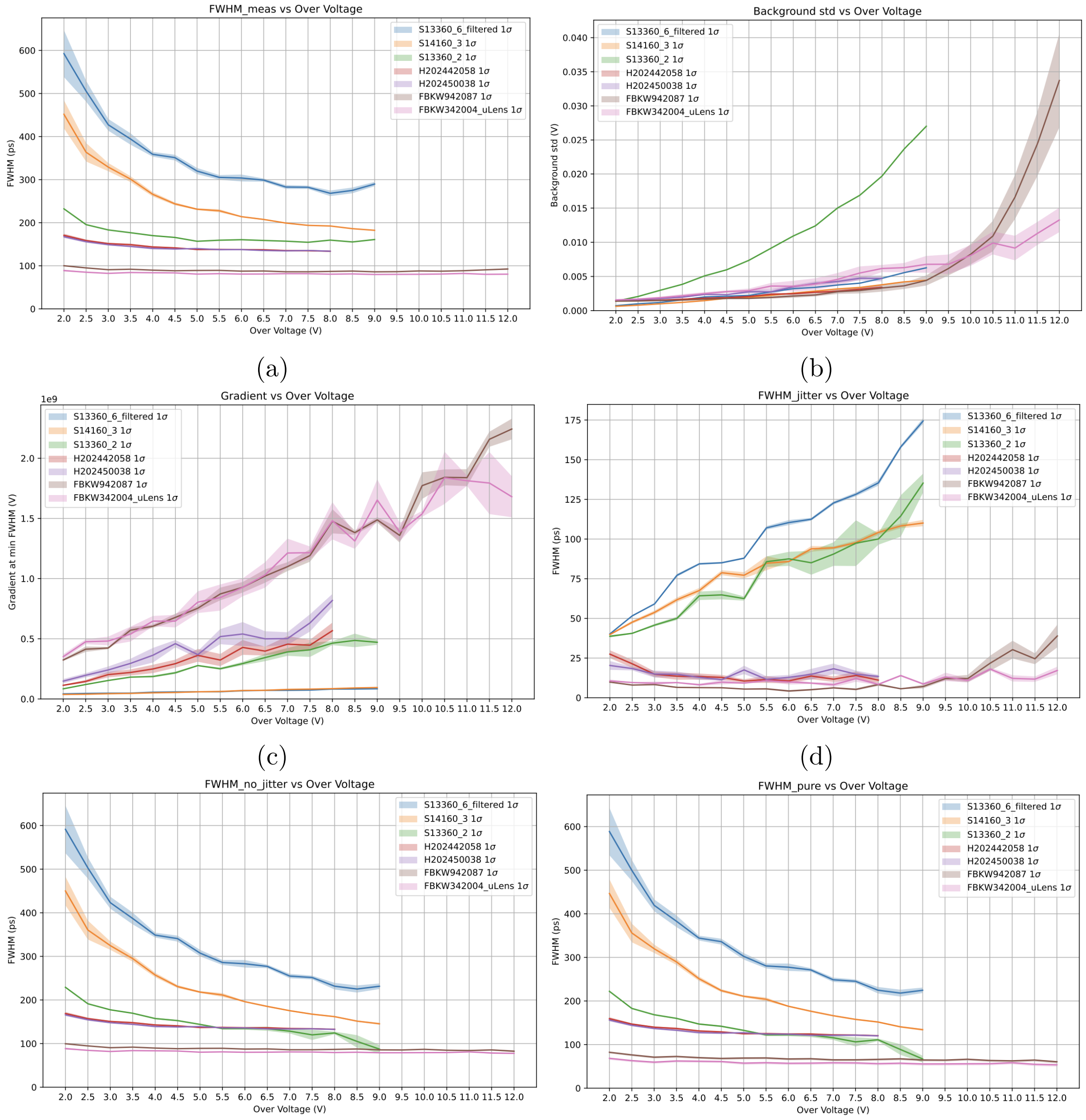

(a) (b)

(c) (d)

(e) (f)

Figure 24: Comparison of timing performance metrics across FBK, Hamamatsu, and Single Channel SiPMs. FBK devices generally exhibit superior timing resolution ($\mathrm{FWHM}_{\mathrm{meas}}$), highest gradients, and lower jitter errors compared to Hamamatsu and Single Channel SiPMs.

(a) FWHM$_{\text{meas}}$: Overall, the FBK SiPMs demonstrate the best timing resolution, followed by the Hamamatsu devices, with the Single Channel SiPMs exhibiting the largest FWHM values. This ranking is consistent across the range of overvoltages (OV) tested.

(b) Background σ: While most channels show similar trends in background noise, the S13360_2 Single Channel SiPM consistently exhibits a higher background standard deviation across the entire OV range. Additionally, the FBKW942087 SiPM shows a pronounced rise in background noise beyond approximately 9.5 V OV.

(c) Signal gradient: The FBK SiPMs maintain the highest signal gradient values, followed by Hamamatsu, with the Single Channel SiPMs showing the lowest gradients. This hierarchy aligns with their overall timing performances.

(d) FWHM$_{\text{jitter}}$: As expected from the background and gradient behaviours, the Single Channel SiPMs generally suffer from larger jitter contributions. In contrast, Hamamatsu and FBK devices have comparable and significantly lower jitter errors.

(e) FWHM$_{\text{no jitter}}$ and (f) FWHM$_{\text{others}}$: After correcting for jitter contributions, FBK SiPMs still lead in timing performance, followed by Hamamatsu, and then Single Channel devices. Interestingly, the S13360_2 device shows a decreasing trend in FWHM values after about 5.5 V OV, eventually outperforming Hamamatsu in this jitter-corrected metric.

Despite being the least advantageous in SPTR, certain Single Channel SiPMs can approach or surpass Hamamatsu performance after accounting for jitter effects, underscoring the importance of detailed noise analysis in evaluating device characteristics.

At 5.0 V overvoltage, a table presenting numerical values for the measured timing resolution (FWHM$_{\text{meas}}$), jitter contribution (FWHM$_{\text{jitter}}$), and other contributions (FWHM$_{\text{others}}$) across the tested SiPM models is shown as Tab. 1.

SiPM	FWHM$_{\text{meas}}$ at 5.0 V	FWHM$_{\text{jitter}}$ at 5.0 V	FWHM$_{\text{others}}$ at 5.0 V
S13360_6_filtered	319.89 ± 7.21 ps	87.95 ± 0.53 ps	$302.43^{+7.37}_{-7.40}$ ps
S14160_3	231.35 ± 2.01 ps	77.18 ± 1.92 ps	$210.79^{+2.16}_{-2.36}$ ps
S13360_2	156.94 ± 0.85 ps	62.48 ± 1.31 ps	$132.62^{+1.00}_{-1.82}$ ps
H202450038	140.05 ± 0.90 ps	17.52 ± 2.64 ps	$127.20^{+0.75}_{-1.75}$ ps
H202442058	137.82 ± 1.53 ps	10.49 ± 1.18 ps	$124.83^{+1.08}_{-1.94}$ ps
FBKW942087	89.19 ± 1.18 ps	5.45 ± 0.29 ps	$69.17^{+0.94}_{-3.10}$ ps
FBKW342004_µLens	80.74 ± 0.53 ps	9.19 ± 0.18 ps	$57.51^{+0.38}_{-0.36}$ ps

Table 1: Numerical values of FWHM$_{\text{meas}}$, FWHM$_{\text{jitter}}$, and FWHM$_{\text{others}}$ at 5.0 V overvoltage for various SiPMs tested, arranged in descending order of SPTR performance.

Hamamatsu SiPMs perform better than Single Channel devices but do not reach the superior timing precision of FBK SiPMs. Among all, the FBKW342004 with microlens stands out as the best-performing sensor, achieving the lowest FWHMmeas and $\mathrm{FWHM}_{\mathrm{others}}$, with relatively low jitter contributions. This superior performance can be attributed to its optimised microcell design and the presence of the microlens, which enhances photon detection efficiency and timing accuracy. The observed ordering and performance trends at 5 V OV are consistent with those at other tested overvoltages, confirming the robustness of these results.

4 Conclusion

In this work, a systematic analysis of the SPTR characteristics is performed for several SiPM devices, including Hamamatsu, FBK, and single-channel models. By decomposing the overall measured timing resolution into contributions from jitter, trigger timing, laser pulse width, and other intrinsic effects, we were able to gain detailed insight into the factors influencing SPTR performance. Our analysis confirmed that FBK SiPMs, particularly the FBKW342004_µLens, outperformed the others due to improved focusing from microlens arrays. Hamamatsu SiPMs showed stable and close-to-optimal SPTR, whereas single-channel SiPMs generally demonstrated inferior timing performance, especially under thermal noise contamination. The introduction of a filtering technique improved the clarity of signal separation in single-channel SiPMs and allowed more accurate extraction of timing metrics.

To further develop our understanding of SPTR in SiPMs, we propose the following future directions:

1. **Better Identification of Single-Channel SiPMs:** The actual model types and parameters of single-channel SiPMs tested were not clearly labeled, leading to uncertainty in performance analysis. Future studies should ensure accurate identification to allow more meaningful comparisons.

2. **Temperature Dependence:** The impact of temperature on SPTR has not been explored in this work. Conducting measurements at lower temperatures may reveal dependencies that can be leveraged for performance optimisation.

3. **Threshold-Dependent FWHM Behaviour:** We observed that the minimum FWHM does not consistently align with the 50% threshold point, where the signal gradient is maximal. The mechanisms behind this deviation merit further investigation.

4. **Physical Interpretation of EMG Fit:** Although the EMG (Exponentially Modified Gaussian) model has been used to describe the time distribution, its physical

basis in relation to photon detection and avalanche formation in SiPMs requires deeper study.

5. **Spatial Contribution to Transit Time Skew:** Future work could involve selectively masking portions of the SiPM active area to assess how spatial photon absorption affects transit time and contributes to intrinsic timing resolution limits.

These directions aim to deepen the understanding of SPTR in SiPMs and facilitate the development of more accurate and efficient photon timing technologies.

References

[1] S. Vinogradov, *The Silicon Photomultiplier (SiPM) Concept and Design Development*, APPEC News, 11 March 2015. Available at: `https://www.appec.org/news/the-silicon-photomultiplier-sipm-concept-and-design-development/`.

[2] *Single-Photon Avalanche Diode (SPADs)*, MeetOptics Academy. Available at: `https://www.meetoptics.com/academy/single-photon-avalanche-diode`.

[3] *Uniform Distribution EXPLAINED with Examples*, YouTube video. Available at: `https://www.youtube.com/watch?v=UC-CBUSQXAo`.

[4] A. Tripathi and M. Shukla, *Physically inspired synthesis of Santoor and Sarod*, in *2015 International Conference on Information and Communication Technology for Intelligent Systems (ICIINFS)*, December 2015. DOI: 10.1109/ICIINFS.2015.7399004.

A Effect of Photon Reflection

We also examined the effect of internal photon reflection by removing the light-absorbing foam from the Faraday box. This led to the emergence of a secondary peak in the time distribution, which is attributed to delayed photon paths from internal reflections. This artifact complicates the fitting with a standard EMG model and illustrates the importance of careful optical isolation in high-precision timing measurements.

For FBKW942087 channel 101, data is taken with or without foam and the measured timing resolution, $\mathrm{FWHM}_{\mathrm{meas}}$, is compared. This allows us to analyse the effect of photon reflection within the Faraday box on the time resolution. The comparison of the $\mathrm{FWHM}_{\mathrm{meas}}$ results is presented in Fig. 25.

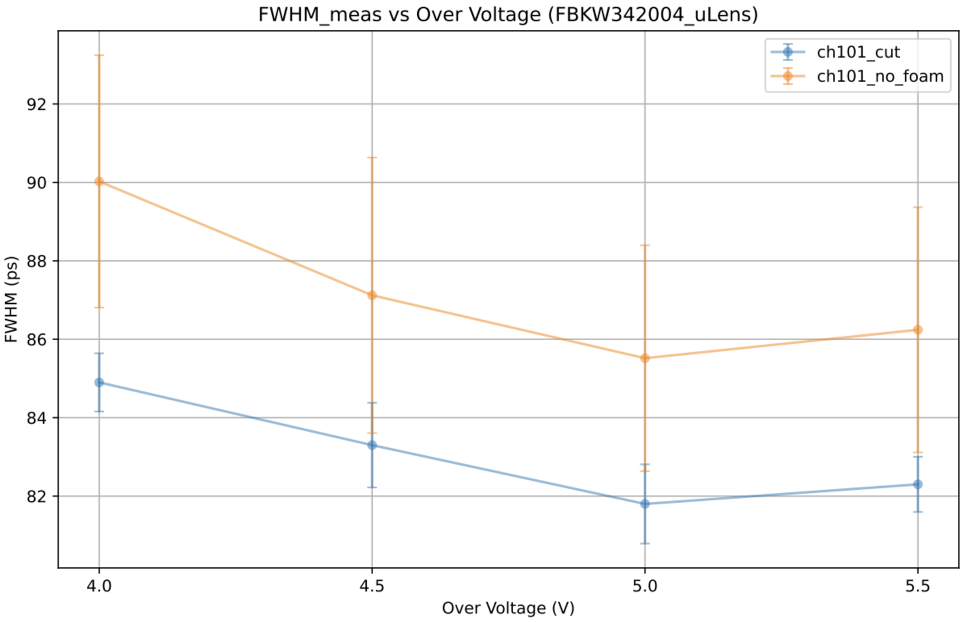

Figure 25: $\mathrm{FWHM}_{\mathrm{meas}}$ of FBKW342004_µLens channel 101 measured with and without the reflection-blocking foam at selected overvoltages.

The data taken without foam shows larger FWHM values and greater errors. This increase is likely due to the contribution of reflected photons within the Faraday box.

The time distributions of the case without foam exhibits a secondary peak, as shown in Fig. 26. This additional peak is not accounted for by the Exponentially Modified Gaussian (EMG) fitting model and is clearly unphysical.

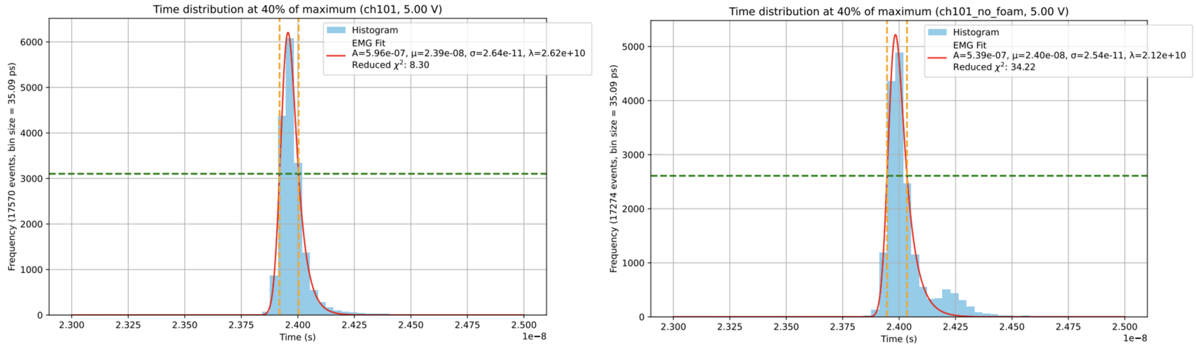

(a) (b)

Figure 26: (a) Time distribution with the foam. (b) Time distribution without the foam. The case without the foam exhibits a secondary peak that cannot be accounted for by the EMG model and is unphysical.

The waveforms corresponding to primary and secondary peaks from Fig. 26b are plotted separately, as shown in Fig. 27. A clear separation between the two peaks becomes evident.

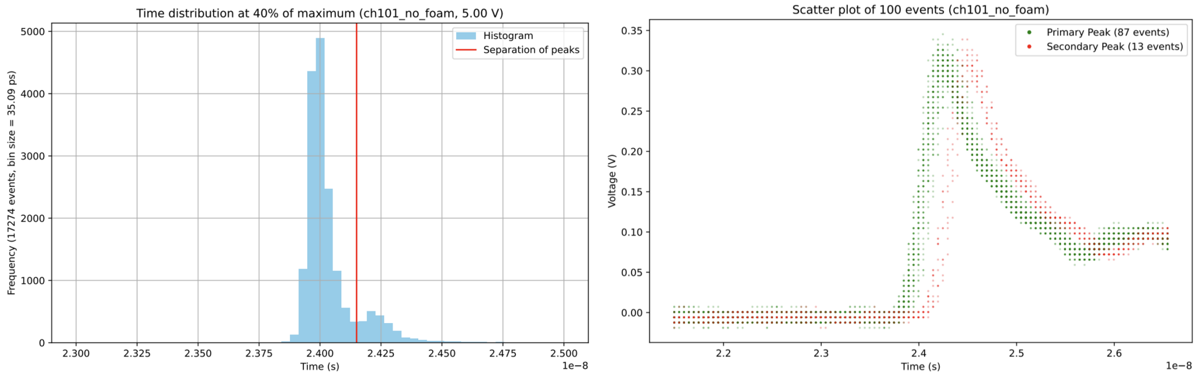

(a) (b)

Figure 27: (a) Separating peaks according to their relative time distribution to reach 40% threshold. (b) Plot of the waveforms related to the two peaks separately. The secondary peak corresponds to a horizontal shift in time of the waveforms.

This distinct separation strongly suggests that the secondary peak arises from delayed photons caused by reflections within the Faraday box. Such reflected photons arrive later than the direct photons, producing the observed secondary peak in the time distribution. This effect highlights the importance of using reflection-blocking foam to ensure accurate timing measurements by minimising photon reflections that degrade the time resolution.